Sensitivity limits on optical gas imaging due to air turbulence

Nathan Hagen*
Utsunomiya University, Center for Optical Research and Engineering (CORE), Department of Optical Engineering, Utsunomiya, Japan

Abstract. Infrared cameras are widely used for the detection of fugitive gas leaks and for quantifying gas emissions. While the gas detection sensitivity in the presence of noise is now well understood, we show that wind-turbulence-induced thermal fluctuations place a fundamental lower limit on gas detection sensitivity. While for many gases the lower limit is too low to be important, we show that for some gases it places a real limitation on measurements when the background is a near-ground surface. [DOI: 10.1117/1.OE.57.11.114102]

Keywords: infrared gas imaging; gas leak detection; turbulence.

Paper 180851 received Jun. 13, 2018; accepted for publication Oct. 23, 2018; published online Nov. 10, 2018.

1 Introduction

With tightening controls on emissions at industrial chemical processing facilities, there is an increasing need for improved gas leak detection equipment and methods. In particular, the high cost of leak detection presents a challenge that many are trying to meet with automated monitoring to replace the current labor-intensive methods.[1] Spectrally filtered infrared cameras have become an indispensable tool for this effort,[2,3] with researchers trying to develop tools to automate the process of detecting and quantifying gas leaks from infrared video data.[4,5]

To detect and measure gas leaks with spectrally filtered infrared cameras, the user looks for changes in the detected thermal radiance while viewing a background scene, searching for patterns that indicate a gas cloud moving across the field of view. Gases that have the strongest absorption cross sections, and whose absorption regions are narrowest, are the easiest to detect, and thus have the lowest detection threshold. In the MWIR (3 to 5 μm), the alkane hydrocarbon gases have strong absorption features and so allow sensitive detection, while in the LWIR (8 to 13 μm), the alkenes allow sensitive detection. Under ideal circumstances, these sensitivities are determined by the signal-to-noise ratio (SNR) of the gas absorption signal to the measurement noise (detector noise plus photon shot noise).[6,7] In practice, however, natural changes in the thermal signature of the scene background is an important nuisance that also interferes with detection. This can result, for example, from the cooling of a sun-illuminated surface after clouds block the sunlight, or simply due to sudden changes in wind speed or direction.

There is another previously unacknowledged effect that interferes with detection—an effect that is particularly problematic because its spatiotemporal behavior is fluid-like. Turbulent wind flow across surfaces induces thermal fluctuations that move with the wind and that can appear similar to flowing gas. These turbulence-induced thermal fluctuations are a phenomenon that has only recently come to attention[8,9] as a method for imaging wind and which create patterns that are visible in trace gas imaging data. Infrared gas imaging and infrared wind imaging both use passive detection in primarily outdoor environments, relying on the same thermal contrast ΔT between the fluid and the background to produce signals. Existing algorithms used for analyzing infrared camera video sequences for gas detection use the fluid-like spatiotemporal behavior to filter out anomalies and reduce false detections. Thus, these turbulence-induced thermal fluctuations will cause false detections if the detection threshold is placed below a lower limit that we estimate quantitatively below. At the sensitivity limit, the small surface thermal fluctuations induced by air turbulence appear as small thermal changes induced by trace gases. This limit is "fundamental" in the sense that it is unrelated to detector or shot noise, has gas-like spatiotemporal behavior, and does not vary with the scene thermal contrast.

In the discussion below, we review the measurement models for infrared gas imaging and wind imaging. Equating the two enables us to calculate the corresponding gas detection sensitivity limits, and we provide example values for various gases in the MWIR and LWIR bands, respectively.

2 Thermal Effects of Wind Turbulence Over a Surface

Figure 1 shows an example scene showing wind-induced thermal fluctuations on a sun-illuminated concrete surface on a warm afternoon. The air temperature for the scene is 35°C, the concrete surface temperature 50°C, and the ambient air at 75% relative humidity. We define the "thermal contrast" of a pixel in the scene as the effective temperature difference between the surface and the ambient air: $\Delta T = T_{\mathrm{bkg}} - T_{\mathrm{air}}$. The camera used for this measurement is an InSb detector array (IRCameras LLC, QuazIR SD) with a 640×512 image size, 20-μm pixels, and 14-bit output at 60 frames/s. The detector is cryocooled to 77 K and operates across the MWIR spectral range with a cold filter transmitting from 3.00 to 3.90 μm. The camera uses an $f/2.3$ lens (Janos Technology Inc., ASIO 50 mm) with a 50-mm focal length. With this configuration, the camera noise-equivalent temperature difference (NETD) is 15 mK, and the integration time is 2 ms.

*Address all correspondence to: Nathan Hagen, E-mail: nh@hagenlab.org

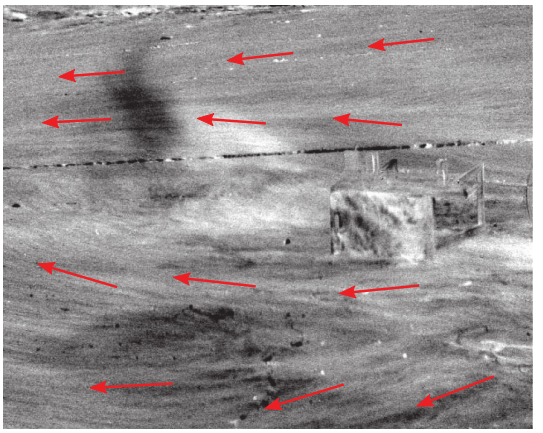

Fig. 1 One frame from a temporally filtered video of a scene composed primarily of solar-illuminated concrete, with some equipment at the center right side of the image. Red arrows indicate the local direction of wind flow along the concrete. The filtered image grayscale display has been linearly scaled to black/white at brightness temperature differences of ±75 mK.

When turbulent cool air passes across a warm surface, some surface regions are briefly cooled by the rapid exchange of (warm) low-velocity air lifted away from the surface with (cool) high-velocity air pushed in toward the surface.[10–12] These small temperature differences δT generally relax over a period of a couple of seconds as the heat conducts into the material beneath the surface.[9]

To visualize the temperature changes δT of objects in a scene down to the several millikelvin level, we can use a simple second-order derivative filter given by the difference between two temporal moving averages:

$$\delta T(x, y) = \langle T \rangle_4 - \langle T \rangle_{80},$$

where $\langle T \rangle_i$ is the time average over i frames. Figures 1 and 2 show the result, where 4 frames and 80 frames correspond to times of 0.067 and 1.33 s, respectively. The short-baseline moving average $\langle T \rangle_4$ is used to reduce noise, while still retaining enough temporal resolution to visualize the thermal fluctuations. Subtracting the long-baseline moving average $\langle T \rangle_{80}$ removes slow thermal drifts, which is important as these drifts tend to dominate over time spans of several seconds or more. Applying these processing steps to an infrared video sequence allows us to visualize the thermal fluctuations in a scene as in Fig. 1. This 20 mK thermal change

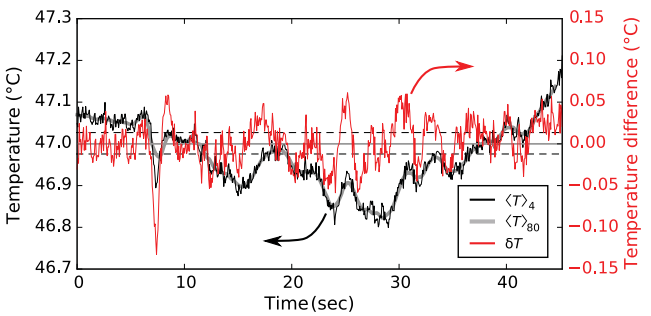

Fig. 2 The temperature history of an example pixel over time, showing $\langle T \rangle_4$ (black line), $\langle T \rangle_{80}$ (thick-gray line), and δT (red line). The dashed lines indicate ±20 mK from the mean.

Table 1 Estimated NETD values for the QuazIR SD MWIR camera imaging different surface temperatures, assuming a surface emissivity of 0.95, with 1, 4, or 80 frames averaged.

Surface temperature (°C)	NETD (mK)	4-frame avg NETD (mK)	80-frame avg NETD (mK)
23	15.0	7.5	1.7
30	14.3	7.2	1.6
50	12.5	6.3	1.4
60	11.7	5.9	1.3

flowing across the field of view can appear as the flow of a trace amount of gas.

A larger air-surface thermal contrast ΔT generates larger thermal fluctuations δT. For outdoor measurements, thermal contrast during the day is usually produced by the absorption of sunlight on a surface, heating it above the temperature of the ambient air. For Fig. 1, a contrast of $\Delta T \sim 15$°C produces thermal fluctuations on the order of $\delta T \sim 20$ mK (Fig. 2). Such a small temperature change is visible to a thermal camera having a rated NETD of 15 mK, because the NETD decreases with higher surface temperatures and also with increasing number of frames averaged as shown in Table 1. On a hot summer day, sunlit concrete often exceeds 50°C, and asphalt pavement can exceed 60°C.[13] These elevated temperatures improve the NETD significantly. If we model the blackbody radiance spectrum of a surface at each temperature, integrated across the detector passband and weighted by the detector responsivity, we obtain the estimated NETD values for various object temperatures shown in Table 1.

Another factor to take into account is the reduction of noise due to summing of multiple frames. Algorithms used for gas imaging typically employ spatiotemporal processing similar to that used for wind visualization—the background scene is assumed to be slowly varying while the gas itself varies over a much shorter timescale. The actual timescales vary with algorithm and with the scale of the leak—imaging small leaks typically requires faster frame rates, and larger leaks lower frame rates. Using a four-frame average as a baseline for the gas layer motion, the NETD will decrease by 2. As a result, for imaging 50°C surfaces with four-frame averaging, the camera NETD decreases to 6 mK, so that the 20 mK turbulence-induced thermal fluctuations become easily visible above the noise (see Table 1).

3 Infrared Gas Imaging

Infrared gas imaging analyzes the radiance changes in a scene to look for absorption or emission signatures generated by gases passing between the camera and the background.[14–17] Gases that are cooler than the background are seen in absorption, while gases warmer than the background (e.g., when passing in front of a cold blue sky) are seen in emission.

We can model the effect of a gas cloud in the scene with a three-layer radiative transfer system (Fig. 3), in which

1. Spectral radiance $L_b(\lambda)$ is generated within a source region that can be either an opaque object such as

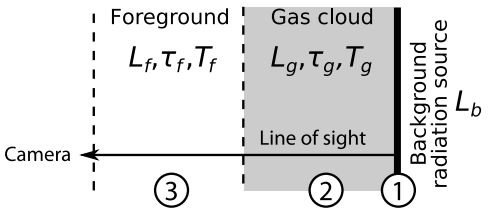

Fig. 3 The measurement geometry for a single pixel in a gas cloud imager: the camera line of sight views the background infrared radiation (1) through a gas cloud layer (2) and a foreground atmospheric layer (3). Each layer has a spectral radiance L, transmission τ, and temperature T.

the ground, or the atmosphere itself, such as when viewing a cloudless sky, or a combination of the two.

2. The source spectral radiance traverses the gas cloud layer, and is attenuated/increased by absorption/emission of gases located there.
3. The radiation passes through an atmospheric layer to reach the camera.

This three-layer model is quite general in that it does not require any assumptions on the spectrum $L_b(\lambda)$ of light behind the gas cloud.[18]

For a pixel in the scene observed by the camera, we can write the radiative transfer equation of a ray along the line of sight to give an at-pupil radiative flux M of

$$\begin{aligned}\overline{M} &= \int_{\lambda_1}^{\lambda_2} \epsilon_f(\lambda)B(T_f,\lambda) + \tau_f(\lambda)\epsilon_g(\lambda)B(T_g,\lambda) \\ &\quad + \tau_f(\lambda)\tau_g(\lambda)L_b(\lambda)\mathrm{d}\lambda \\ &\approx \Delta\lambda[\overline{\epsilon_f}\,\overline{B}(T_f,\lambda) + \overline{\tau}_f\overline{\epsilon_g}\,\overline{B}(T_g) + \overline{\tau}_f\overline{\tau}_g\overline{L}_b],\end{aligned} \tag{1}$$

where the subscripts f, g, and b indicate the foreground, gas, and background layers; λ_1 and λ_2 give the passband of the infrared filter; $B(T)$ is the Planck blackbody spectral radiance function for temperature T; τ is the spectral transmission of a layer; and ϵ the spectral emissivity of a layer. An overbar indicates an average across the spectral passband. Using Kirchhoff's law and an assumption of local thermodynamic equilibrium, we can make the substitution $\epsilon = 1 - \tau$. The overbars on parameters become tedious, and so we will drop them in the equations below, leaving the average over the passband implied, except for parameters in which an explicit wavelength dependence is shown.

For gas cloud imaging, we look for radiance changes in the scene that may indicate absorption or emission by a gas cloud by comparing the current frame against a reference gas-free frame. We can use spatiotemporal statistics of the spectrum to determine the presence of gas and to estimate the reference radiance value. Writing the radiance of the current frame of a video sequence as M_1 and that of the reference frame as M_0, we have

$$\begin{aligned}M_0 &= (1-\tau_f)B(T_f) + \tau_f L_b \\ M_1 &= (1-\tau_f)B(T_f) + \tau_f\tau_g B(T_g) + \tau_f\tau_g L_b.\end{aligned}$$

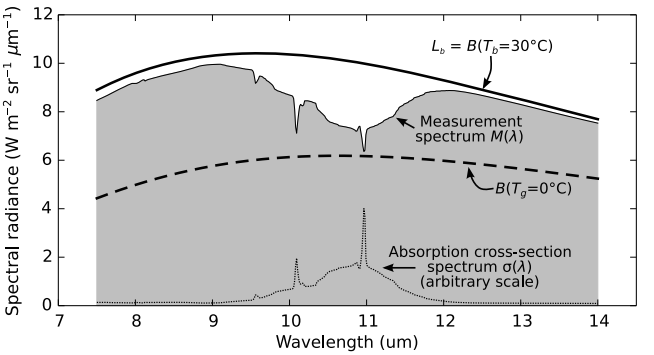

Fig. 4 Example spectra for propylene gas at column density $\zeta = 22000$ ppm.m, showing the radiance spectrum $M(\lambda)$ when the background source is a blackbody at $T_b = 30$°C.

Taking the difference between the two spectra gives

$$\Delta M = M_1 - M_0 = -\tau_f\alpha_g[B(T_g) - L_b]. \tag{2}$$

Figure 4 shows $\alpha_g(\lambda)$ for propylene gas, together with an example $\Delta M(\lambda)$ for a background blackbody at 30°C and a 0°C gas passing between it and the camera. Rearranging Eq. (2) to solve for the gas absorption, we obtain

$$\alpha_g = \frac{M_1 - M_0}{\tau_f[B(T_g) - L_b]}. \tag{3}$$

The denominator of this equation has the gas-to-background radiance contrast $\Delta L = [B(T_g) - L_b]$, a quantity that is closely related to the thermal contrast ΔT. From Eq. (2), we can use the gas-free frame to solve for L_b:

$$L_b = \frac{1}{\tau_f}[M_0 - [1-\tau_f]B(T_f)],$$

and substitute the result into Eq. (3) to give

$$\alpha_g = \frac{M_1 - M_0}{B(T_g) - M_0}. \tag{4}$$

Note that τ_f has disappeared from the equation: the foreground layer plays no role in the absorption estimate, except insofar as it reduces the measurement SNR. All of the variables on the right-hand side of this equation are quantities that we can measure or estimate.

To convert the measured absorption to gas column density, we use the Beer–Lambert–Bouguer law:

$$\tau_g(\lambda) = \exp\left[-\sigma(\lambda)\int_0^{\ell}\rho(z)\mathrm{d}z\right] \approx \exp(-\sigma\rho\ell), \tag{5}$$

where $\sigma(\lambda)$ is the absorption cross-section spectra, ℓ is the line-of-sight path length through the gas, and $\tau = 1 - \alpha$. We use $\rho(z)$ for the gas concentration (number density) along the line of sight and ρ (with no explicit z-dependence) as the average concentration along the line of sight. Because the average concentration ρ and gas cloud path length ℓ cannot be separated from one another, they are grouped together into a single quantity—the column density $\zeta = \rho\ell$.

When the gas concentration is low (thin gas approximation), Eq. (5) can be written as $\alpha_g \approx \sigma\zeta$—the gas column

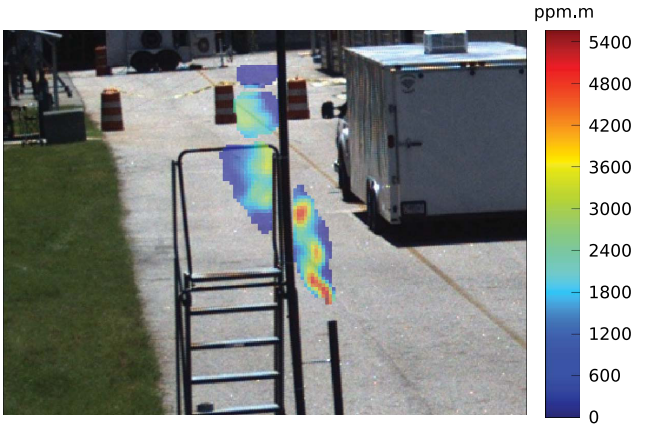

Fig. 5 Example gas detection image. (Adapted with permission of Rebellion Photonics, Inc.[21])

density ζ becomes a linear function of the absorption. Going from the estimated absorption to estimated gas column density, therefore, requires only scaling by the cross section:

$$\zeta = \alpha_g/\sigma. \tag{6}$$

The column density has units of m^{-2}, but it is common to convert this to units of ppm.m by multiplying by the density of molecules in air ($\rho_{air} = 2.687 \times 10^{25}$ m^{-3} at standard temperature and pressure), and scaling the result by 10^6.[19,20] Figure 5 shows an example of applying this estimation to each pixel of gas in an image, for a controlled methane gas leak.

4 Calculating the Bandpass-Averaged Absorption Cross Section

For spectrally filtered gas imaging cameras, the filter design directly impacts measurement performance, and there are trade-offs to consider when selecting the filter passband. One generally wants to have an absorption cross section as large as possible, so that for many spectra a naive choice would be to design a narrowband ($\lesssim$10 nm) filter centered on a strong absorption line feature, such as the narrow peak at 10.97 μm in Fig. 4. While this works for laser-illuminated systems, it gives poor performance for passive imagers because the background signal SNR becomes too low. By widening the filter passband, we increase the background SNR, but we sacrifice the highest absorption cross section as the measured absorption will be an average across the entire passband. In practice, one can achieve good SNR for passbands wider than about 0.1 μm.

In addition to trading-off the absorption cross section for increased background SNR, the filter design must also consider that absorption features with cross sections below 1.0×10^{-25} m^2 are of limited utility in typical measurement environments. Here, the trade-off is that when we include spectral regions with low absorption cross section, we are increasing the measurement shot noise while doing little to increase the absorption signal. For $\bar{\sigma} \lesssim 1.0 \times 10^{-25}$ m^2, this balance typically tips in the favor of rejecting light in that range.

The final consideration for filter design is that we will only investigate the case of single-passband filters. Multiband filters can be used for optimizing the average cross section when the absorption spectrum has multiple peaks, such as propane and butane have in the LWIR (Fig. 6). However, these are specialized items that are not in common use in the infrared.

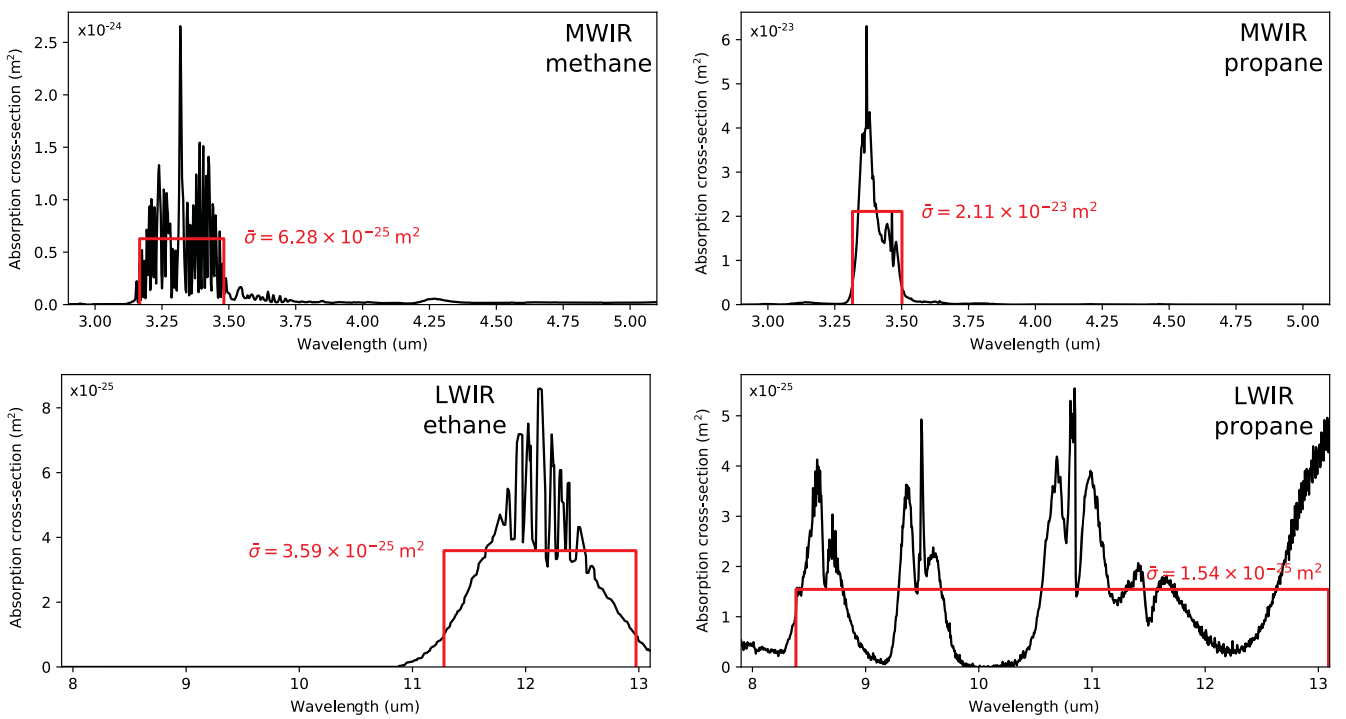

Fig. 6 Absorption spectra for methane and propane in the MWIR, and ethane and propane in the LWIR. The horizontal red line indicates the width of the suggested bandpass filter to use for detecting the gas, while the vertical position of the line indicates the average cross section within that passband.

Table 2 Turbulence-induced lower limits for gas sensitivity.

	MWIR			LWIR		
Gas	Filter bandpass (μm)	σ (m^2)	Sensitivity lower limit (ppm.m)	Filter bandpass (μm)	σ (m^2)	Sensitivity lower limit (ppm.m)
Ammonia	2.90 to 3.42	2.62×10^{-25}	185	10.31 to 10.86	4.73×10^{-24}	10.2
Benzene	3.20 to 3.31	4.90×10^{-24}	9.88	9.41 to 9.89	1.07×10^{-24}	45.1
n-butane	3.33 to 3.51	2.76×10^{-23}	1.75	9.91 to 10.75	8.16×10^{-25}	59.3
Isobutylene	3.21 to 3.52	1.31×10^{-23}	3.70	10.67 to 11.77	9.93×10^{-24}	4.87
Ethane	3.26 to 3.51	4.74×10^{-24}	10.2	11.28 to 12.98	3.59×10^{-25}	135
Ethylene	3.12 to 3.40	1.08×10^{-24}	45.0	10.12 to 10.66	5.39×10^{-24}	8.98
Methane	3.17 to 3.48	6.28×10^{-25}	77.0	7.90 to 8.22	4.17×10^{-25}	116
Propane	3.32 to 3.50	2.11×10^{-23}	2.29	8.38 to 13.10	1.54×10^{-25}	313
Propylene	3.19 to 3.52	2.48×10^{-24}	19.5	9.78 to 11.61	2.33×10^{-24}	20.8
SO_2	2.90 to 5.10	4.36×10^{-25}	111	7.90 to 10.02	1.08×10^{-24}	44.8

Implementing a simple filter design that considers these trade-offs gives the resulting passbands shown in Fig. 6 and Table 2. The thick red horizontal line in each figure indicates the suggested filter passband appropriate to optimizing the measurement performance of the imaging system for that gas.

5 Detection Limits

In Sec. 2, we showed that in conditions of thermal contrast $\Delta T \sim 15$°C, we observe air-turbulence-induced surface thermal fluctuations of about 20 mK, which traverse the scene at the same speed as the airflow. A gas detection camera will see these thermal fluctuations as apparent changes in gas layer absorption, so that if we place a gas detection threshold that is too low, these thermal fluctuations will appear as tendrils of gases flowing across the scene. To estimate the threshold at which this occurs, we can convert the thermal fluctuations into absorption units α_{limit}, from which we can use [Eq. (6)] to calculate the equivalent column density ζ_{limit} for any given gas type.[22] This gives us the lower sensitivity limit for the gas.

For these measurement conditions, we find the apparent absorption:

$$\alpha_{\text{limit}} = \frac{\delta M}{\Delta M} \approx \frac{\delta T}{\Delta T} = \frac{0.020\ \text{K}}{15\ \text{K}} = 0.0013. \tag{7}$$

Although this apparent absorption is calculated for a reference scene thermal contrast of $\Delta T = 15$°C, both the turbulence and gas signals vary linearly with thermal contrast for typical values of ΔT, so that the ratio used to calculate α_{limit} is approximately invariant to scene conditions. Thus, a scene contrast of only 5°C will produce thermal fluctuations of about 7 mK, resulting in the same α_{limit} value of 0.0013.

The following gives an example calculation for the case of methane gas in the MWIR. The average absorption cross section of methane gas in the 3.17- to 3.48-μm range is $\sigma = 6.28\times10^{-25}$ m^2 (see Table 2 for gas absorption cross sections). By scaling the apparent change in absorption to a corresponding change in apparent gas column density, we obtain the detection sensitivity limit for methane as

$$\begin{aligned}\zeta_{\text{limit}} &= \left(\frac{\alpha_{\text{limit}}}{\overline{\sigma}}\right)\left(\frac{1\times10^6\ \text{ppm}}{\rho_{\text{air}}}\right)\\ &= \left(\frac{0.0013}{6.28\times10^{-25}\ \text{m}^2}\right)\left(\frac{1\times10^6\ \text{ppm}}{2.69\times10^{25}\ \text{m}^{-3}}\right)\\ &= 77\ \text{ppm.m}.\end{aligned} \tag{8}$$

Performing the same calculation for propane in the LWIR, we obtain the sensitivity limit of

$$\begin{aligned}\zeta_{\text{limit}} &= \left(\frac{0.0013}{1.54\times10^{-25}\ \text{m}^2}\right)\left(\frac{1\times10^6\ \text{ppm}}{2.69\times10^{25}\ \text{m}^{-3}}\right)\\ &= 313\ \text{ppm.m}.\end{aligned} \tag{9}$$

The results for the same calculations, performed in the MWIR and LWIR for several common hydrocarbon gases, are shown in Table 2. As gas imaging cameras have difficulty in detecting column densities <10 ppm.m, we can see from Table 2 that only ammonia, methane, and ethylene experience a sensitivity limit in the MWIR band that could potentially restrict performance. In the LWIR band, the gases tend to have lower absorption cross sections, so that propane, ethane, and methane have detection limits that impose a significant limit on detection. In practice, this can be seen as an anomalous increase in false-detections across the field of view when trying to image propane at the bottom limit of detectability. This limit does not change with larger thermal contrast because the turbulence effects also increase linearly with ΔT. In practice, we also find that wind speed has little effect on the detection limits because the primary effect of an increase in wind speed is to reduce the thermal contrast.

Although these detection limits are prevalent in gas imaging, they are not present everywhere. The turbulence-

induced thermal fluctuations are only apparent on nearby surfaces, so that any gas imaging that uses a distant background, such as sky, clouds, or mountains, is not subject to these limits. In addition, the calculations of Table 2 ignore the effects of water vapor on the absorption spectra. This particularly affects the cross section of methane in the LWIR as the absorption spectrum partially overlaps with the water absorption spectrum. As a result, the sensitivity limit will depend on the local temperature and relative humidity.

6 Conclusions

Wind passing over the ground produces dynamic thermal fluctuations that follow wind speed and direction. Trace quantities of infrared gases passing across the field of view create subtle spatiotemporal patterns that can be used to detect gas leaks. Analyzing these two effects together, we have shown that the thermal signatures induced by air turbulence create a fundamental lower limit on the ability to detect trace gases with infrared imaging, independent of measurement noise. Although researchers have shown that LWIR detection limits for uncooled infrared imaging cameras under good measuring conditions are generally in the region of 50 to 1000 ppm.m for many of the common hydrocarbon gases, and 1000 to 5000 for propane,[4,7,23] temporal averaging while staring at a scene containing gas can bring down these limits by a factor of 10 or more. At these lower limits, however, any gas having a small absorption cross section ($\lesssim 2 \times 10^{-25}$ m^2) will start to encounter limitations due to the turbulence effects. Thus, imaging propane gas with LWIR cameras will experience difficulties for propane column densities below about 300 ppm.m. Practical experience with trying to measure propane in the LWIR reinforces this—researchers have not yet succeeded in consistently imaging propane at levels near this value when the camera uses a nearby surface for background. These sensitivities have been reached when imaging propane in the LWIR against a blue sky background because the turbulence effects do not apply there, and because blue sky also provides a strong thermal contrast for measurement. This gives two good reasons to choose an upward-viewing geometry for imaging propane leaks in the LWIR: better contrast and lack of turbulence fluctuations.

While the calculations of Table 2 focus on a filtered camera model for measurement, spectral imaging cameras have also become increasingly common for gas sensing. The advantage of a spectral imager is that it can analyze the signal change in multiple bands simultaneously, allowing it to see the difference between a broadband spectral change (such as that generated by the turbulence-induced fluctuations) and a spectral change that has a shape specific to a given gas. Thus, a spectral imager can make use not only of the spatiotemporal distribution of intensity changes to detect gas clouds, but can also use the correlation between the measured absorption spectrum with the known gas spectrum. As a result, spectral instruments will be less susceptible to the turbulence-induced fluctuations affecting their detection limits.

References

1. D. W. Furry et al., "Evaluation of instrument leak detection capabilities for smart LDAR application: chemical plant testing," *Environ. Progr.* **26**, 197–205 (2007).
2. Eastern Research Group, "Spectral testing of gas imaging cameras and spectral library," Summary Report prepared for U.S. EPA, Office of Enforcement and Compliance Assistance, Air Enforcement Division, EPA Contract No. EP-W-09–033, Work Assignment ETS-2–1 (ERG), Rev. No. 2 (2014).
3. D. R. Lyon et al., "Aerial surveys of elevated hydrocarbon emissions from oil and gas production sites," *Environ. Sci. Technol.* **50**(9), 4877–4886 (2016).
4. N. Hagen et al., "Video-rate spectral imaging of gas leaks in the long-wave infrared," *Proc. SPIE* **8710**, 871005 (2013).
5. H. Abdel-Moati et al., "New optical gas-imaging technology for quantifying fugitive-emission rates," in *Int. Petroleum Technology Conf.*, IPTC-18471-MS (2015).
6. D. F. Flanigan, "Vapor-detection sensitivity as a function of spectral resolution for a single Lorentzian band," *Appl. Opt.* **34**(15), 2636–2639 (1995).
7. E. Naranjo, S. Baliga, and P. Bernascolle, "IR gas imaging in an industrial setting," *Proc. SPIE* **7661**, 76610K (2010).
8. A. Inagaki et al., "Thermal image velocimetry," *Boundary Layer Meteorol.* **149**(1), 1–18 (2013).
9. N. Hagen, "Passive imaging of wind surface flow using an infrared camera," *Infrared Phys. Technol.* **87**, 47–54 (2017).
10. B. J. Cantwell, "Organized motion in turbulent flow," *Ann. Rev. Fluid Mech.* **13**, 457–515 (1981).
11. J. Jiménez, "Turbulent flows over rough walls," *Ann. Rev. Fluid Mech.* **36**, 173–196 (2004).
12. G. Kawahara, "Theoretical interpretation of coherent structures in near-wall turbulence," *Fluid Dyn. Res.* **41**(6), 064001 (2009).
13. T. Asaeda, V. T. Ca, and A. Wake, "Heat storage of pavement and its effect on the lower atmosphere," *Atmos. Environ.* **30**, 413–427 (1996).
14. D. F. Flanigan, "Prediction of the limits of detection of hazardous vapors by passive infrared with the use of MODTRAN," *Appl. Opt.* **35**(30), 6090–6098 (1996).
15. J. Sandsten, H. Edner, and S. Svanberg, "Gas visualization of industrial hydrocarbon emissions," *Opt. Express* **12**(7), 1443–1451 (2004).
16. A. Ben-David and C. E. Davidson, "Probability theory for 3-layer remote sensing radiative transfer model: univariate case," *Opt. Express* **20**(9), 10004–10033 (2012).
17. S. Sabbah et al., "Remote sensing of gases by hyperspectral imaging: system performance and measurements," *Opt. Eng.* **51**(11), 111717 (2012).
18. M. A. Rodríguez-Conejo and J. Meléndez, "Hyperspectral quantitative imaging of gas sources in the mid-infrared," *Appl. Opt.* **54**(2), 141–149 (2015).
19. N. B. Gallagher, B. M. Wise, and D. M. Sheen, "Estimation of trace vapor concentration-pathlength in plumes for remote sensing applications from hyperspectral images," *Anal. Chim. Acta* **490**(1–2), 139–152 (2003).
20. S. Niu et al., "New approach to remote gas-phase chemical quantification: selected-band algorithm," *Opt. Eng.* **53**(2), 021111 (2014).
21. https://rebellionphotonics.com/.
22. N. Hagen, "Millikelvin thermal dynamics of infrared scenes: sensitivity limits on optical detection of gas leaks," *Proc. SPIE* **10403**, 104030G (2017).
23. S. E. Golowich and D. G. Manolakis, "Cramer-Rao bounds for long-wave infrared gaseous plume quantification," *Opt. Eng.* **53**, 021109 (2014).

Nathan Hagen is an assistant professor at Utsunomiya University. He received his BS degree in physics and astrophysics from the University of California at Berkeley in 1993 and his PhD in optical sciences from the University of Arizona in 2007. From 2011 to 2016, he led the research and algorithms group at Rebellion Photonics, developing spectral imaging cameras for gas detection and quantification. He has authored 30 journal articles and is a member of SPIE.